



OPEN ACCESS

EDITED BY

Malgorzata Holyńska,
European Space Research and Technology
Centre (ESTEC), Netherlands

REVIEWED BY

Omid Sharifahmadian,
Alexander Dubcek University in
Trencin, Slovakia
Sivashankar Krishnamoorthy,
Luxembourg Institute of Science and
Technology (LIST), Luxembourg

*CORRESPONDENCE

Daniel Wyn Müller,
✉ daniel.mueller@uni-saarland.de

RECEIVED 08 March 2024

ACCEPTED 04 July 2024

PUBLISHED 30 July 2024

CITATION

Müller DW, Josten B, Wältermann S, Pauly C,
Slawik S, Brix K, Kautenburger R and
Mücklich F (2024), Microstructure versus
topography: the impact of crystallographic
substrate modification during ultrashort
pulsed direct laser interference patterning on
the antibacterial properties of Cu.
Front. Mater. 11:1397937.
doi: 10.3389/fmats.2024.1397937

COPYRIGHT

© 2024 Müller, Josten, Wältermann, Pauly,
Slawik, Brix, Kautenburger and Mücklich. This
is an open-access article distributed under
the terms of the [Creative Commons
Attribution License \(CC BY\)](https://creativecommons.org/licenses/by/4.0/). The use,
distribution or reproduction in other forums is
permitted, provided the original author(s) and
the copyright owner(s) are credited and that
the original publication in this journal is cited,
in accordance with accepted academic
practice. No use, distribution or reproduction
is permitted which does not comply with
these terms.

Microstructure versus topography: the impact of crystallographic substrate modification during ultrashort pulsed direct laser interference patterning on the antibacterial properties of Cu

Daniel Wyn Müller^{1,2*}, Ben Josten¹, Sebastian Wältermann^{1,2},
Christoph Pauly¹, Sebastian Slawik¹, Kristina Brix³,
Ralf Kautenburger³ and Frank Mücklich¹

¹Department of Materials Science, Saarland University, Saarbrücken, Germany, ²SurFunction GmbH, Saarbrücken, Germany, ³Department of Inorganic Solid-State Chemistry, Elemental Analysis, Saarland University, Saarbrücken, Germany

Introduction: Topographic surface patterning in the micro- and nanometer scale has evolved into a well applied approach in surface functionalization following biomimetic blueprints from nature. Depending on the production process an additional impact of process-related substrate modification has to be considered in functional surface optimization. This is especially true in case of antimicrobial applications of Cu surfaces where a modification of the substrate properties might impact bactericidal efficiency.

Methods: In this regard, the effect of ultrashort pulsed direct laser interference patterning on the microstructure of pure Cu and resulting antimicrobial properties was investigated alongside line-like patterning in the scale of single bacterial cells.

Results and Discussion: The process-induced microstructure modification was shown to play an important role in corrosion processes on Cu surfaces in saline environment, whereas the superficial microstructure impacts both corrosive interaction and ion emission. Surprisingly, antimicrobial efficiency is not predominantly following deviating trends in Cu ion release rates but rather depends on surface topography and wettability, which was shown to be impacted by the substrate microstructure state, as well. This highlights the need of an in-depth understanding on how different surface properties are simultaneously modulated during laser processing and how their interaction has to be designed to acquire an effective surface optimization e.g., to agitate active antimicrobial surface functionalization.

KEYWORDS

direct laser interference patterning, antimicrobial surfaces, biomimetic surface structures, ultrashort laser pulses, antibacterial Cu

1 Introduction

While the need for improved decontamination measures has become painfully aware to the public during the recent pandemic, biofilm prevention has already been an increasing issue in numerous technical and medical applications before. In 2019, the damage caused by biofilms was estimated to run up to 4,000 billion USD, majorly comprising technical impairment with a share of approx. 66% solely related to corrosion and 20% to the health sector (Cámara et al., 2022). In parallel, biofilm related health issues become increasingly severe with the ongoing emerge of antimicrobial resistances in pathogenic microorganisms, where multi-resistant bacteria have even been found in the most remote habitats (Sobisch et al., 2019).

Concepts to control the microbial load of technical and hygienic surfaces has been in the focus of research for decades aiming to prevent severe material deterioration as well as a spread of pathogens in multiple environments (Mikolay et al., 2010; Zea et al., 2020; Siems et al., 2022). The most common approaches on antimicrobial surfaces are following a strategy of either contact guiding up to repulsion to avoid initial microbial seeding or active killing mechanisms. Periodic surface patterns that scale slightly below single bacterial cells have been found to reduce the overall bacterial surface loads for certain tested bacteria strains (Peter et al., 2020). This has been shown to be most effective against several gram-negative bacteria species, whereas a universal applicability of the repelling topography effect cannot be established (Fadееva et al., 2011; Epperlein et al., 2017). Following the natural blueprints of topographies found on dragonfly and cicada wings, nm-scaled surface asperities can also be designed to induce a rupture of bacterial cell membranes (Tripathy et al., 2017). However, a supporting role of secondary functional surface properties such as wettability, which introduces attractive forces or external drag has to be considered here to drive the mechanical mode of action (Tripathy et al., 2017; Boinovich et al., 2018). Such physico-chemical surface properties have in fact repeatably been shown to be highly involved in bacteria/surface interaction (Pratt and Kolter, 1998; Kimkes and Heinemann, 2020; Maikranz et al., 2020).

Applying active antimicrobial agents like Copper (Cu) and Silver (Ag), the state of the surface has to be similarly considered since the deactivation of adherent microorganisms is directly related on the quantitative emission of toxic ions (Hans et al., 2014; Meister et al., 2022). On Cu surfaces, effective ion emission has been shown to be negatively affected by thermally induced oxide layers, with a corresponding decrease in antimicrobial efficiency against *Escherichia coli* (Hans et al., 2013). A similar effect was observed on Cu based surfaces after different methods of laser processing, whereas a change in alloy stoichiometry could also be determined to play an important role (Boinovich et al., 2019; Ahmed et al., 2023). Variations in surface finishing on pure Cu surfaces has been shown to cause different states of surface deformation and grain fining down to nm-scales where antimicrobial efficiency could be impacted by enhanced Cu ion release. Here, the superficial microstructure of Cu has been shown to be modified by polishing routines (Luo et al., 2019a), surface processing via spray-coating and shot peening (Razavipour et al., 2022). Consequently, rapid bacterial killing rates on Cu surfaces have recently been achieved by an significant increase

of initial Cu emission by means of a porous surface design that aims for a high surface/volume ratio (Smith et al., 2022).

Further approaches to improve antimicrobial properties of Cu surfaces aim for a combination of the active toxicity induced killing effect with e.g., mechanical surface functionalization by involving the surface concepts of dragonfly or cicada wings (Emelyanenko et al., 2020; Yi et al., 2021). However, the gain of the additional mechanic killing effect is associated with losses in Cu ion release due to the chemical surface modification of the structuring methodology used (Hans et al., 2013; Boinovich et al., 2019).

In a recent study, the antimicrobial efficiency of Cu surfaces against *E. coli* have been improved by applying periodic surface patterns in the scale of single bacteria cells via ultrashort pulsed direct laser interference patterning (USP-DLIP) (Müller et al., 2021). Increased bactericidal activity was associated with both topographic and physico-chemical surface modification, where a process-induced impact on the substrate properties was also evident. This antimicrobial surface concept is currently investigated in the ISS flight experiments BIOFILMS and Touching Surfaces (Siems et al., 2022). In this context, the objective of this study is to provide a detailed analysis of how USP-DLIP processing alters the functional surface properties of Cu surfaces, which may be associated with their active antimicrobial mechanisms with a particular focus on crystallographic substrate modification. Analyzation involves X-ray diffraction (XRD), energy dispersive X-ray spectroscopy (EDS) and electron back-scatter diffraction (EBSD) aside of different imaging modes of scanning electron microscopy (SEM) including focused ion beam cross-sectioning (FIB-SEM). Assessment of the resulting functional surface properties is conducted via contact angle (CA) measurement and wet plating experiments monitoring the antimicrobial properties against *E. coli*. The dissection of process-induced influences on the superficial microstructure and related antimicrobial activity allows for an improved comprehension of the complementing effects of the various functional surface properties impacted by USP-DLIP to further enhance antimicrobial efficiency of Cu surfaces.

2 Materials and methods

2.1 Material preparations and USP-DLIP

Oxygen-free Cu (>99.95% purity, provided in sheets of 1 mm thickness from Wieland, Germany) was cut to coupon sizes of $10 \times 25 \text{ mm}^2$. Surface finishing of the Cu samples was executed following a stepwise procedure involving fine grinding on 1200 grit silicon carbide paper and polishing by three consecutive steps (6 μm , 3 μm , 1 μm diamond suspension with decreasing pressure of 15 to 10 N) that results in a roughness $R_a < 10 \text{ nm}$. Between each polishing step, a thorough cleaning with distilled water and ethanol is conducted to remove suspension remnants. At this point, one share of the as-polished samples additionally underwent annealing for 12 h at 450°C and 10^{-7} mbar in a vacuum furnace followed by electropolishing [as described in (Lößlein et al., 2021)] to provide Cu substrates without microstructure deformation from cold-roll processing of the Cu sheets and mechanical surface deformations from polishing. Another share of both as-polished and annealed

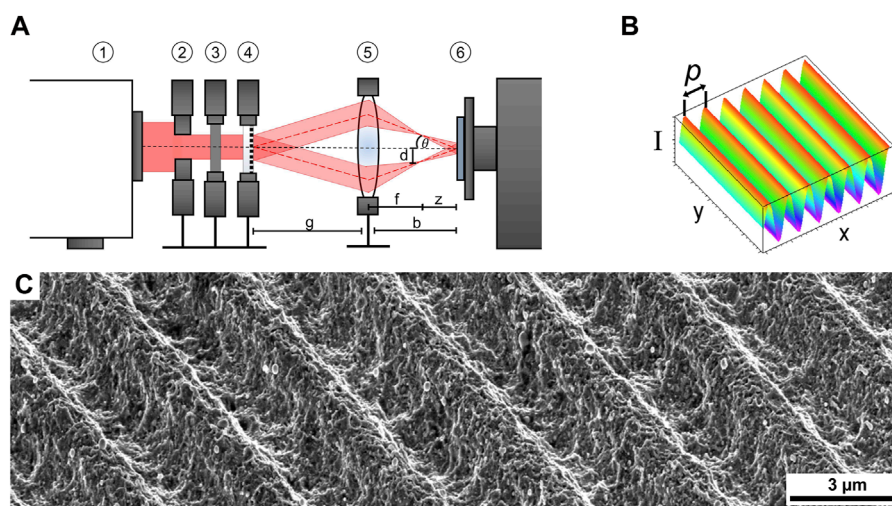


FIGURE 1
(A) optical Setup used for USP-DLIP: 1 laser source, 2 aperture, 3 waveplate, 4 DOE, 5 lens system, 6 sample on x-, y- motion stage. **(B)** intensity pattern resulting from two beam interference. **(A, B)** have been adapted with permission from Müller et al. (2020a). **(C)** SEM image of USP-DLIP patterned surface in SE contrast at 52° sample tilt.

samples is held back to be used as reference surfaces in the further experiments.

Topographic surface patterning was conducted via USP-DLIP at a pulse duration τ_p of 100 fs at Full Width Half Maximum (FWHM) and centered wavelength λ of 800 nm using a *Ti:Sapphire* laser system (*Spitfire, Spectra Physics*). In the optical DLIP setup illustrated in Figure 1A (Müller et al., 2020a), a wave plate is used to adjust the polarization of the seed beam, which is further separated into two partial beams by a diffractive optical element (DOE). A multi-lens system finally superimposes the separated partial beams on the substrate surface. This induces two-beam laser interference in which the individual beams are p-polarized in orientation to the line-like interference pattern (illustrated in Figure 1B). The setup of both the DOE and multi-lens system adjusts the single beam incidence angle θ , by which the pattern periodicity P can be defined according to Eq. 1.

$$P = \frac{\lambda}{2 \sin(\theta)} \quad (1)$$

In this study, a partial beam incidence angle of $\theta = 7.66^\circ$ was applied resulting in a fixed pattern periodicity of 3 μm . Cu surfaces were processed by scanning the sample surface in continuous pulsing mode at a fluence of 2.1 J/cm² and 1 kHz pulse frequency. The pulse overlap was tuned to a spatially agglomeration pulse count of $N = 10$ by adjusting x- and y-hatching according to (Müller et al., 2020a). The resulting surface topography is shown in Figure 1C).

Both as-polished as well as annealed Cu samples underwent USP-DLIP processing (laser structured LS and heat treated before laser structuring HT-LS), from which a third share of LS samples is extracted to be annealed as described above. This results in topographically patterned surfaces without mechanically deformed microstructure (laser structured, then heat treated, LS-HT). Process-induced surface oxidation of the USP-DLIP samples was removed for half of the sample batches via immersion etching in 3% citric acid for 1 minute in an ultrasonic bath

[according to (Müller et al., 2020b)]. This further allows analysis in an as-processed and naturally passivated surface state after etching (LS-E, HT-LS-E, and LS-HT-E).

From this procedure, a matrix of Cu surface states is gained that vary in topography, microstructure and the oxidic passivation layer (listed in Table 1), which allows for investigation on their individual impact on antimicrobial surface properties.

2.2 Surface wettability

Contact angle (CA) measurements were conducted on each sample type listed in Table 1 after 3 weeks of aging in ambient conditions. In this passivation state, surface wettability alteration after surface treatment via mechanical/electro-polishing, annealing or USP-DLIP processing can be considered as mostly stabilized (Löflein et al., 2022). The static contact angle of distilled water was monitored in triplicates at a fixed droplet volume of 3 μL by means of a Drop Shape Analysator DSA 100 (*Krüss GmbH*). The CA was measured both in orthogonal and parallel sample orientation to also include anisotropic droplet propagation in case of the line-like surface patterns.

2.3 Wet plating

Escherichia coli K12 WT(BW25113) was cultured according to the protocol provided by Molteni et al. (2010) by aerobic overnight growth in Lysogeny broth (LB) medium at 37°C and 220 rpm shaking speed. The stationary cells were collected from 5 mL culture medium by centrifugation for 15 min at 5000 \times g. The final bacteria testing solution (BTS) was gained by washing the collected cells in three similar consecutive centrifugation steps followed by resuspension, each in 5 mL of phosphate buffered saline (PBS) with

TABLE 1 Surface states of the different sample types.

Sample type	Topography	Microstructure	Passivation layer
polished	flat	cold-roll + polishing deformation	natural
annealed		without microstructure deformation	natural
LS	patterned in relation to single bacterial cell size	cold-roll + polishing deformation + USP-DLIP induced surface defects	USP-DLIP induced
LS-E			natural
HT-LS		only USP-DLIP induced surface defects	USP-DLIP induced
HT-LS-E			natural
LS-HT		without microstructure deformation	after annealing (10^{-7} bar)
LS-HT-E			natural

a pH value of 7.4. The initial average cell count following this routine ranges in the scale of 9 log CFU/mL. Prior to wet plating, the bacteria were stored at 4°C on Agar plates, which were provided by the group of Prof. Rolf Müller from the Helmholtz Centre of Infection Research, Saarbrücken.

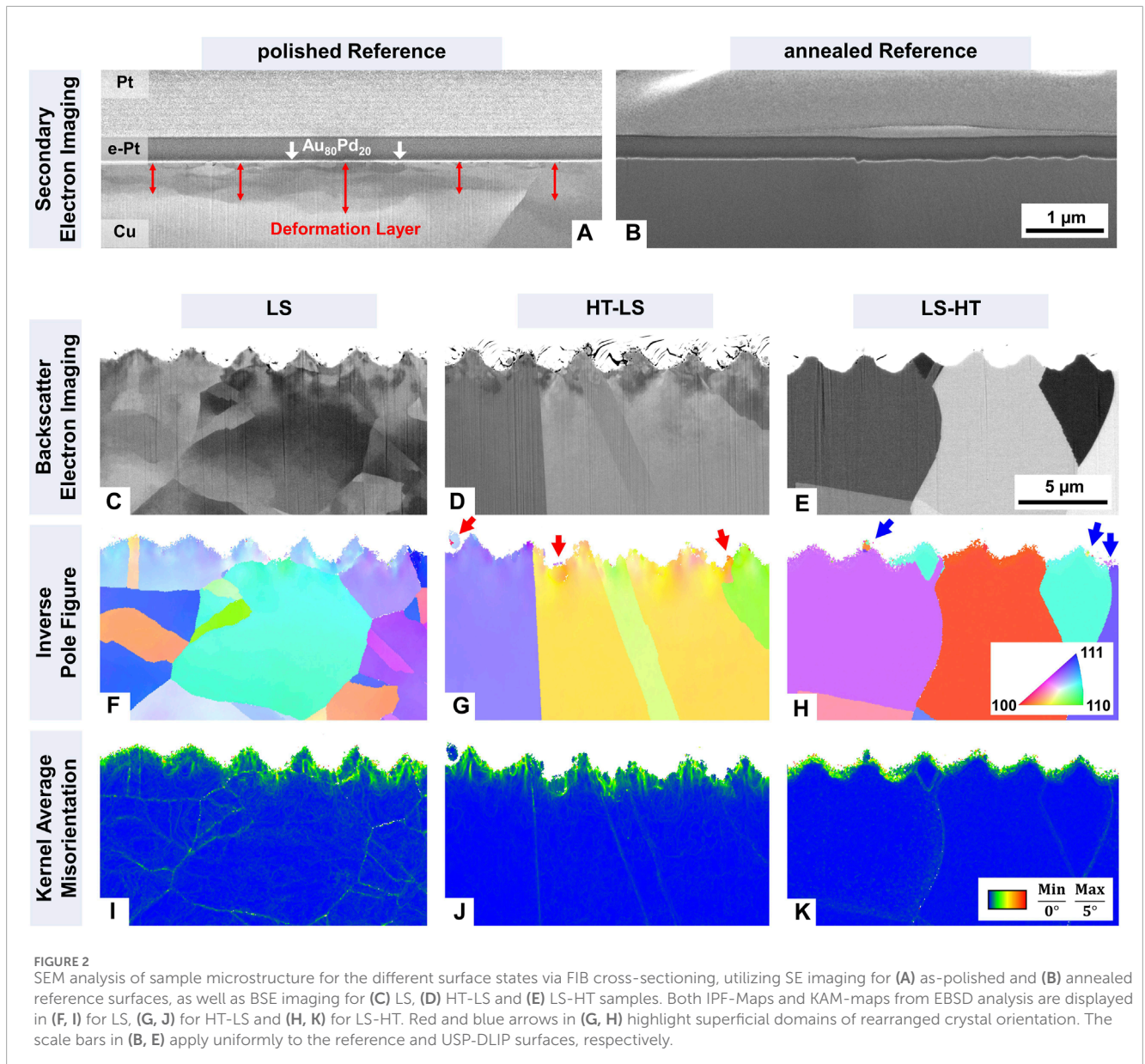
To enable a homogeneous exposure area on the individual samples despite heterogeneous surface wetting properties, droplets of 40 µL of the BTS were applied in predefined areas within polyvinyl chloride (PVC) rings exhibiting an inner circular diameter of 5 mm (Müller et al., 2021). The slightly hydrophobic PVC prevents BTS from spreading on hydrophilic and facilitates droplet covering of the predefined area on hydrophobic surfaces. During the experiment, the samples were stored in water saturated environment at ambient temperature. After three exposure intervals of 30, 60, and 90 min, two doses of 5 µL were withdrawn probing a different droplet for each interval. Surface adherent bacteria were resuspended by vigorous pipetting in parallel orientation to the surface pattern to avoid bacterial retention by topographic shadowing within the pattern valleys. Assessment of the viable bacterial cell numbers was conducted by the standard plate count method following serial 2 log dilution of a single 5 µL BTS dose in PBS and spreading on LB agar plates. To enable counting of the remaining colony forming units (CFU), the inoculated agar plates were incubated overnight at 37°C and 80% moisture. The second 5 µL dose was diluted 600-fold in 0.1% HNO₃ followed by analysis via inductively coupled plasma triple quadrupole mass spectrometry (ICP-QQQ, Agilent 8900) to determine the Cu ion concentration within the BTS corresponding to the parallelly monitored CFU values.

Complementary to BTS exposure, a second set of wet plating experiments was conducted utilizing PBS solution without *E. coli* to assess differences in corrosion behavior of the individual surface states related to the presence of bacteria.

2.4 Characterization

Characterization of the USP-DLIP surface topography was conducted by means of confocal laser scanning microscopy (LSM)

utilizing a *LEXT OLS4100 3D Measuring Laser Microscope* by *Olympus* (50× lens, 2x and 6x increased magnification, laser wavelength 405 nm) to assure conformity of the patterned sample types. Detailed analysis of the individual surfaces was applied via scanning electron microscopy (SEM) including characterization in both secondary and back-scatter electron contrast (SE, BSE) as well as focused ion beam cross-sectioning (FIB) and electron back-scatter diffraction (EBSD). High-resolution SE imaging in immersion mode was used for both surface and cross-section imaging using the system's in-lens detector (*Helios Nanolab600* by *FEI*). Analyzation involved both the initial surface state as well as corrosion damage and passivation layer formation after exposure within the wet plating experiments. For FIB cross-sectioning, the investigated surface site was covered with a protective layer of electron and ion beam induced Pt-deposition to prevent ion-induced degradation of the substrate surface. An additional contrast layer of ~10 nm Au₈₀Pd₂₀ was previously applied via sputter coating to distinguish between original surface features and the Pt-layers (highlighted in Figure 2A). Measurement of passivation layer thickness was conducted using *ImageJ (Fiji)* (Schneider et al., 2012). BSE imaging by means of a solid-state detector was used in combination with EBSD to visualize the sub-surface microstructure within single cross-sections (*Helios PFIB G4 CXe* by *Thermo Fisher*). For both SE and BSE, an acceleration voltage of 5 kV was applied. Surface imaging in SE contrast was conducted at a sample tilt of 52° degree for improved visualization of topographical features. FIB cross-sectioning was executed at 30 kV beam current for both Ga- and Xe-ion beams. EBSD measurements were carried out at 20 kV acceleration voltage and a beam current of 26 nA using a high-speed CMOS camera (*Velocity Super* by *EDAX*) set to a 4 × 4 binning. For EBSD analysis, neighboring domains were measured on a hexagonal grid with a step size of 50 nm. EBSD patterns were recorded and processed using the Neighbor Pattern Averaging and Reindexing (NPAR) algorithm in *OIM Analysis 8.6* software by *EDAX* to improve indexing rate and reduce orientation noise. Thereafter, lattice planes oriented parallel to the cross-section surface were extracted. From the data, both Inverse Pole Figure (IPF) maps in relation to the sample normal of the analyzed surface



and Kernel Average Misorientation (KAM) relative to the next neighbors were taken for depth related analysis of superficial deformation states.

To assess the initial as well as the post-exposure phase and grain deformation state of the different surface types, X-ray diffraction (*PANalytical X'Pert PRO-MPD*) utilizing Cu K_{α} radiation was applied in both Bragg-Brentano (BB-XRD) and grazing incidence (GI-XRD) geometry at a grazing angle of 1° with a Goebel mirror as primary optics. In these parametrizations, 95% of the measured signal is originating from substrate depths of approx. $12 \mu\text{m}$ (Cu 111) to $24 \mu\text{m}$ (Cu 311) in case of BB-XRD and $<1.1 \mu\text{m}$ for GI-XRD according to Cullity and Stock (2001). The diffraction plane was oriented parallel to the line-like patterns to avoid topographic shadowing of the valley surface compartments.

3 Results and discussion

3.1 Initial surface state

The initial surface state of the individual sample types was analyzed by means of SEM/FIB - USP-DLIP processed samples additionally underwent EBSD analysis - as well as BB-/GI-XRD and CA measurement to determine both crystallographic and functional surface properties. In case of the reference surfaces, SE imaging of FIB cross-sections displays a deformation layer of approximately 500 nm depth ($496 \pm 238 \text{ nm}$) in case of the mechanically polished Cu surface, which is absent on the additionally annealed samples (see Figures 2A, B).

Based on the DLIP parametrization chosen, line-like surface patterns have been generated on the differently pretreated Cu

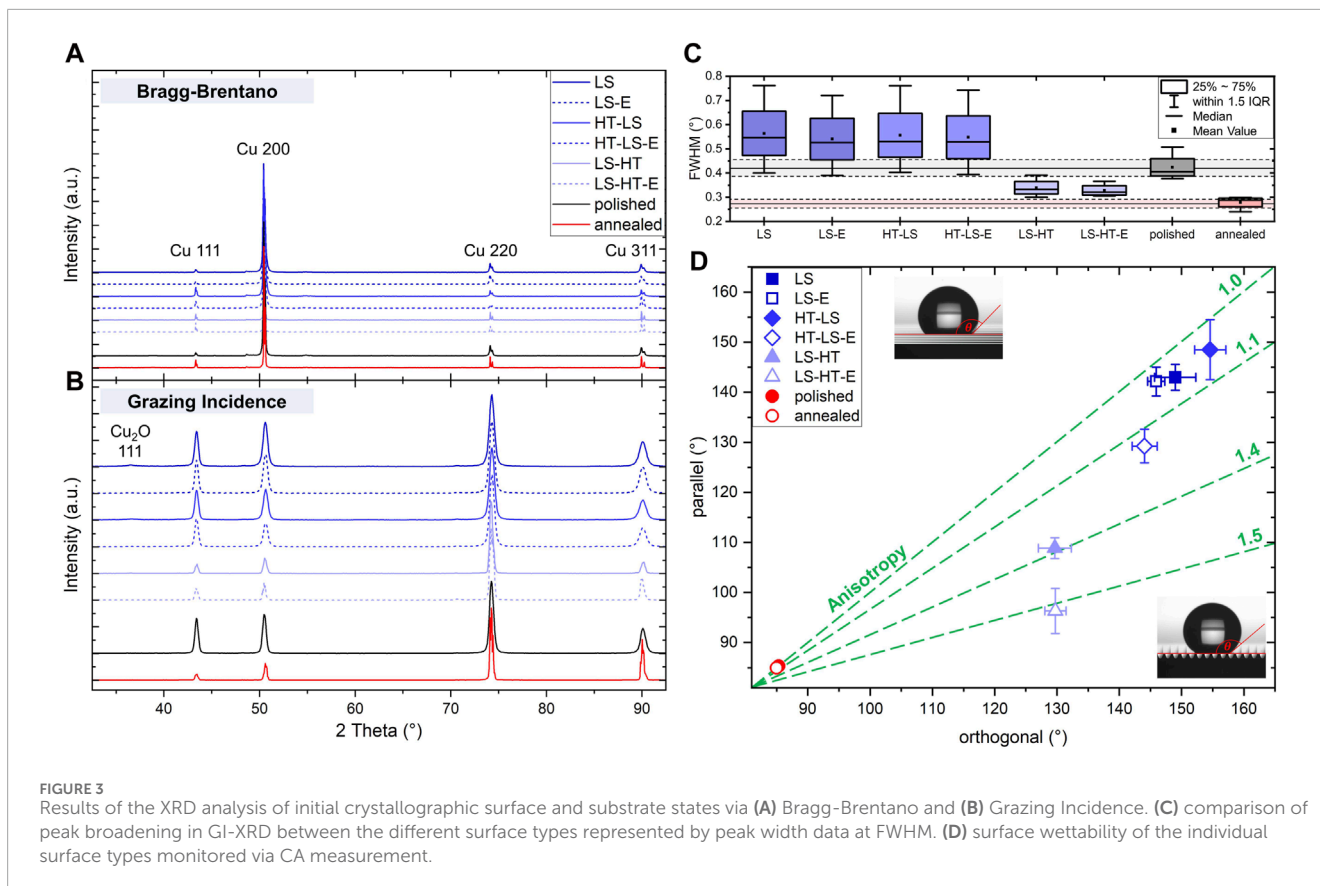
surfaces that exhibit trench widths of approx. $2.13 \pm 0.09 \mu\text{m}$ and depths of approx. $0.97 \pm 0.1 \mu\text{m}$. The applied fluence of 2.1 J/cm^2 induces substrate ablation dominated by phase explosion kinetics, which was previously been shown to impact the superficial substrate crystallography by mechanically as well as thermally induced defect implantation (Xiong et al., 2017; Müller et al., 2023). The resulting laser induced modification of the substrate microstructure was visualized via FIB cross-sectioning by means of the orientation contrast in BSE imaging as well as EBSD. Cross-sections of LS samples exhibit intragranular orientation gradients that can be related to the cold-rolled state of the Cu sheets. The annealed sample types HT-LS and LS-HT do not show variations in intragranular orientation contrast but a marginally increased grain size, instead (compare Figures 2C–E). In the surface vicinity of HT-LS samples, a deformation layer originating from USP-DLIP processing is exhibited, which intersects with the intragranular contrast alterations of the cold-rolled substrate in case of LS. Accordingly, a comparable microstructure state can be observed in the micropatterned surface areas for LS and HT-LS surface types via EBSD examination. This is indicated both by color-gradients in IPF-mapping, as well as low angle orientation misorientations visualized in KAM-maps that can be related to geometrically necessary dislocations (GND) (displayed in Figures 2F, G, I, J). In contrast, ultimately annealed LS-HT surfaces do not exhibit misorientations within the bulk substrate. Here, EBSD analysis of both LS and HT-LS samples indicates a predominant impact of laser processing on the superficial microstructure state that additionally adds to preexisting deformation layers. In superficial areas, minor domains of crystallographic reorientation can additionally be observed in IPF-mapping (examples marked in Figure 2G with red arrows). Smaller domains of rearranged crystal orientation of previously deformed surface compartments during annealing are visible within the topographic surface features of the LS-HT sample type in Figure 2H (blue arrows). In the LS-HT cross-sections, misorientations determined via KAM are limited to the pattern surfaces without loop shaped progressions into the substrate interior, which indicates a possible link to boundary artifacts of the misorientation measurement on the intersection between substrate surface and covering layers of Pt (Figure 2H).

Monitoring the texture state of the differently processed near surface volumes via BB-XRD reveals a predominant peak intensity for 200 oriented lattice planes parallel to the surface that is linked to the cold-rolled initial Cu surface state (see Figure 3A). Annealing does not impact this characteristic texture, whereas a slight increase of the Cu 111 integral intensities can be observed in comparison to the LS and polished reference surfaces. Based on these observations, USP-DLIP processing does not appear to have a significant effect on the state of bulk Cu microstructure in depths $>12 \mu\text{m}$. A process-related impact on functional substrate properties might therefore be predominantly related to superficial defect implantation in smaller depths. With a shallower signal depth of approx. $1.1 \mu\text{m}$ (95% of the signal intensity), peak dominance shifts to Cu 220 in GI-XRD with a more pronounced deviation between the different surface states (visible in Figure 3B). For both polished and LS samples, Cu peak integral intensities scale as $111 < 200 < 220$ in similar magnitude. This characteristic relation is amplified after annealing with a preferential increase of the 220 intensity as visible for LS-HT samples as well as the annealed reference. Since the sample irradiation angle

is fixed in GI-XRD, the measured spectrum does not show grain orientation distribution in parallel orientation to the sample surface, whereas different mostly complex indicated orientations contribute to the individual peaks. However, in the GI-parametrization applied here, Cu grains with a preferred crystal orientation 111 parallel to the substrate surface exhibit a 220 plain orientation that might contribute to the GI-Cu 220 signal due to a close angle relation. By this, the increase of the Cu 111 peak in BB-XRD analysis might at least partially contribute to the increasing Cu 220 dominance in GI-XRD for annealed Cu surfaces. USP-DLIP processing of annealed surfaces in case of HT-LS again induces higher 111 and 200 signals in GI-XRD, however with inverted relation in comparison to polished and LS surfaces, which might be linked to crystallographic adaption mechanisms like twinning following plastic deformation (Vincenc Oboňa et al., 2014; Zhao et al., 2014; Xiong et al., 2017).

Comparing the individual laser processed surface states before and after immersion etching exhibits a neglectable impact of post-processing on Cu substrate crystallography, while the previously visible Cu_2O 111 peak related to process-induced oxidation vanishes for LS and HT-LS samples (visible in Figure 3B). Peak broadening can already be observed visually for polished in comparison to annealed reference surfaces in Figure 3B with relation to a higher deformation state, similarly applicable in LS, HT-LS vs. LS-HT comparison. Considering the peak width deviation at FWHM between the individual deformed surfaces states, peak broadening can be observed for the USP-DLIP processed sample types LS and HT-LS compared to the polished reference indicating a higher overall deformation state (see Figure 3C). The annealed USP-DLIP samples LS-HT and LS-HT-E exhibit higher peak broadening than the respective annealed reference sample as well, but scale below the polished reference.

The impact of microstructure modification aside of topographic remodeling during USP-DLIP on functional surface properties was assessed by CA measurements after 3 weeks of aging under ambient conditions. At this stage, surface passivation involving monolithic oxide growth and agglomeration of carbon species can be assumed to have reached mostly stabilized conditions. In case of the line-like USP-DLIP surface topographies, wetting behavior can be assessed by both the quantitative CA values and droplet shape anisotropy. Due to the pattern geometry, droplets tend to get pinned on the pattern peaks, while they can extend along the pattern trenches with lesser topographic resistance leading to an elongation parallel to pattern orientation in case of higher hydrophilicity. Accordingly, a mild CA drop in orthogonal orientation to the pattern is always accompanied by increasing droplet anisotropy, since the simultaneous decrease in parallelly oriented CA is more significant. Comparing surface wettability of the different patterned surface states indicates a dominant impact of laser-induced substrate modification, whereas both the LS and HT-LS sample types exhibit high CA and low anisotropy close to the super-hydrophobic wetting regime, while LS-HT surfaces exhibit lower hydrophobicity accompanied by increasing droplet anisotropy, as visible in Figure 3D. Immersion etching also affects surface wettability indicated by decreasing CA, however with a lower impact compared to laser-induced substrate deformation. The effect of



crystallographic defect density on CA can also be seen for the reference surfaces, however on a significantly lower scale. Based on this, process induced microstructure modification alongside USP-DLIP appears to play an at least similarly important role in modifying surface wettability than the actual topographic surface modification. A recent study observed similar relations between the superficial defect state of Cu substrate microstructure and surface wetting in case of polished surface topographies where a quicker increase in hydrophobicity was linked to higher chemical activity of surfaces that exhibit higher defect densities (Lößlein et al., 2023).

3.2 Antibacterial efficiency against *E. coli*

Wet plating was conducted on samples that underwent 3 weeks of aging under ambient conditions corresponding to the functional surface properties previously described. The intervals for probing were selected to enable continuous monitoring of the reduction in bacteria viability, while still detecting a count of viable bacteria after the longest exposure duration on most surfaces. This approach intends to enable a better comparison of antimicrobial efficiency between the different Cu surfaces despite deviating interaction under BTS exposure.

Each of the Cu surfaces exhibit high antimicrobial properties, with a >99.9% reduction of viable bacteria cell count already being assessed after 60 min of exposure independent of the surface preparation routine (see the line graph in Figure 4A). Within this

time interval, contact killing on USP-DLIP surfaces is surpassing the references leading to final CFU reduction rates after 90 min that scale between one and three orders of magnitude higher (indicated by the bar graph in Figure 4A). Comparison of CFU reduction between as-processed and immersion etched samples exhibit higher antimicrobial efficiency of the former within the differently processed USP-DLIP surface types. LS and immersion etched HT-LS samples exhibit an initial lag phase within the first 30 min of exposure that shows an inverted relation to their respective CA-values. A similar effect was previously monitored in a comparable experiment, where lower initial CFU reduction was linked to yet developing surface wetting on highly hydrophobic surfaces which delays initial bacteria/surface contact (Müller et al., 2021). Both LS-HT sample types do not show this initial lag phase, where lower CA values and high droplet anisotropy indicate an early initial surface wetting in the Wenzel state. However, the as-processed HT-LS samples do not seem to follow this relationship. They exhibit initial killing rates that indicate well-expressed initial surface wetting in contrast to the high CA values measured. Considering the different bacteria/surface contact states in the initial experiment phase due to a still developing surface wetting of the BTS droplet on USP-DLIP samples, CFU values after 90 min of exposure might provide the most suitable indication of actual differences in bacterial killing of the different surface states. Here, CFU reduction levels are of the same order of magnitude between the majority of laser processed surface types, with reduction rates normalized to similar surface/area ratio that scale between 2.5 and 7.5 times higher than the reference surfaces (bar graph in Figure 4A).

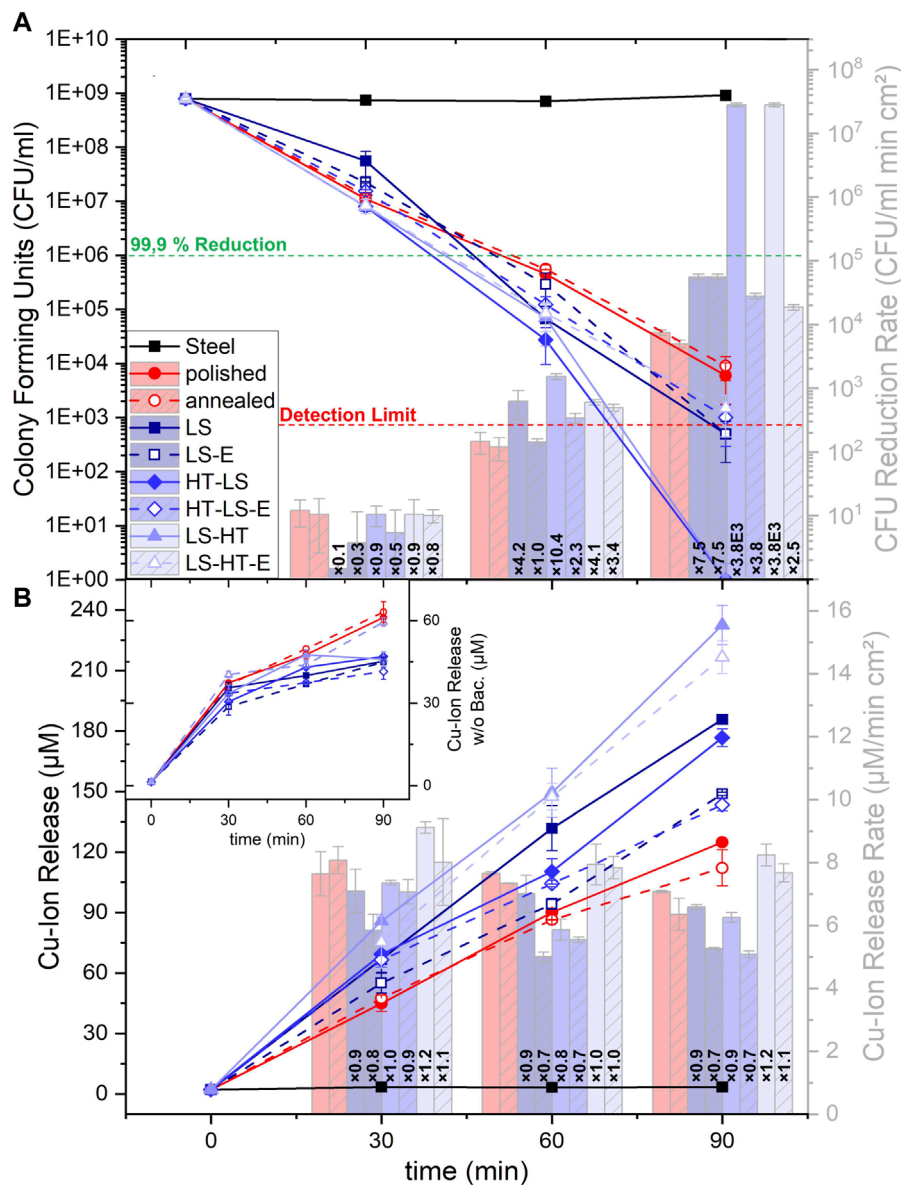


FIGURE 4 Graphical reproduction of the results from the wet plating experiments on the different sample types: (A) Bacterial killing monitored via the assessment of the viable cell count (CFU) after 30, 60 and 90 min of exposure (line graph), with a normalization of the assessed data to homogeneous surface ratios representing the time dependent killing rate (bar graph). (B) parallelly detected Cu ion release (line graph), also normalized in surface area and time dependency (bar graph). The inlay graph represents Cu ion release measured for PBS exposure without inoculated bacteria.

Between the immersion etched surface states, the highest killing efficiency measured is shifted from LS-HT to LS between 60 and 90 min of exposure, which is however not observed for the as-processed samples. It has to be mentioned that the abrupt decrease of measured CFU for both HT-LS and LS-HT after 90 min of exposure is most likely linked to the close vicinity of the measured values to the detection limit of the CFU counting methodology for low amounts of viable bacteria. Thereby, the actual viable bacterial count might range closer to the values of the LS surface type in a similar relation like the deviation range between the final CFU values of the immersion etched USP-DLIP surface types.

In contrast to the variable progression of the CFU values, Cu ion release exhibits an almost stable ratio between the different surface types throughout extended exposure. Normalizing the measured values to surface area ratio and exposure time, a slight decline in the Cu release rate over time can be uniformly visualized which is most pronounced for HT-LS samples after 30 min of exposure (see Figure 4B). The quantitative Cu emission throughout BTS exposure scales higher on USP-DLIP surfaces in comparison to the smooth references (represented in the line graph in Figure 4B). Here, as-processed USP-DLIP surfaces tend to exhibit a higher Cu ion release compared to their immersion etched counterpart, where in each case ion emission measured on LS and HT-LS surfaces

appear to be closely related. The normalized values presented in the bar graph of Figure 4B reveal a lower $\mu\text{M}/\text{cm}^2$ relation of both USP-DLIP surface types to the reference surfaces. LS-HT surfaces in turn exhibit the highest overall ion release values both with and without surface/area ratio normalization, by which Cu ion release in $\mu\text{M}/\text{cm}^2$ scales as LS-HT > references > LS, HT-LS.

Surface exposure to PBS without inoculated bacteria exhibits an inverted relation of Cu emission between the USP-DLIP and reference samples, whereas LS-HT surfaces retain high release values close to the references (visible in Figure 4B inset). The Cu ion release measured on the as-polished and annealed reference samples is inverted, as well. The barely observable decline in Cu ion release after 30 min of exposure to BTS is well pronounced in case of PBS exposure, especially on LS and HT-LS surfaces. The overall quantity of ion release accumulated after 90 min of exposure remains below the values of BTS exposed surfaces with a two-fold decrease for the reference and a 3.3 to 5 fold decrease for the USP-DLIP surface types.

The monitored difference in Cu emission with and without bacteria inoculation highlights a catalytic effect of bacterial presence on corrosive processes on Cu surfaces, independent of the deformation state of the superficial microstructure or surface wettability. Similar observations have previously been made (Luo et al., 2019b; Emelyanenko et al., 2020), where Luo et al. (2019b) stated that bacteria play an active role in Cu corrosion by draining the solution of Cu ions, which impairs the formation of oxides and thus surface passivation. This has also been linked to an alteration in quantitative ion release in a previous work, where USP-DLIP samples exhibit a higher surface passivation than mirror-polished surfaces under exposure to pure PBS (Müller et al., 2021). A similar relation can be found in the results presented in Figure 4B, where Cu ion release measured under exposure to PBS with and without bacteria inoculation exhibits an alteration that is more pronounced for USP-DLIP surfaces than the corresponding behavior on reference surfaces. Quantitative Cu emission is similar between USP-DLIP surfaces, but in inverted relation to the reference surfaces. Here, Cu ion release between LS and HT-LS samples can be assumed to follow similar corrosion mechanisms due to closely related values in both experiments. The combination of a lower Cu ion release rate under BTS exposure, as well as continuously reduced emission in contact to pure PBS observed on these surfaces indicates increased passivation capacities in comparison to both LS-HT and the reference surfaces.

Aside of a uniform increase, bacterial killing does not present a clear relation to actual Cu ion release on the topographically patterned surfaces. Although having the second highest Cu emission, immersion etched LS-HT samples exhibit the lowest CFU reduction rate after 90 min of exposure. On the other hand, the relation of bacterial killing between LS and HT-LS in the immersion etched state is closely linked to the corresponding ion emission slopes, while the overall difference in contact killing between as-processed and immersion etched surface states extends in the same way to their ion release ratios, as well. Here, the high initial killing on as-processed HT-LS also corresponds to a peaking Cu ion release rate within the first 30 min of BTS exposure. In similar relation, the higher killing rates on as-polished in comparison to annealed reference surfaces are paralleled by a slightly higher Cu ion release. The differences in bacterial killing after 90 min of exposure appear to be more consistently related to the corresponding CA

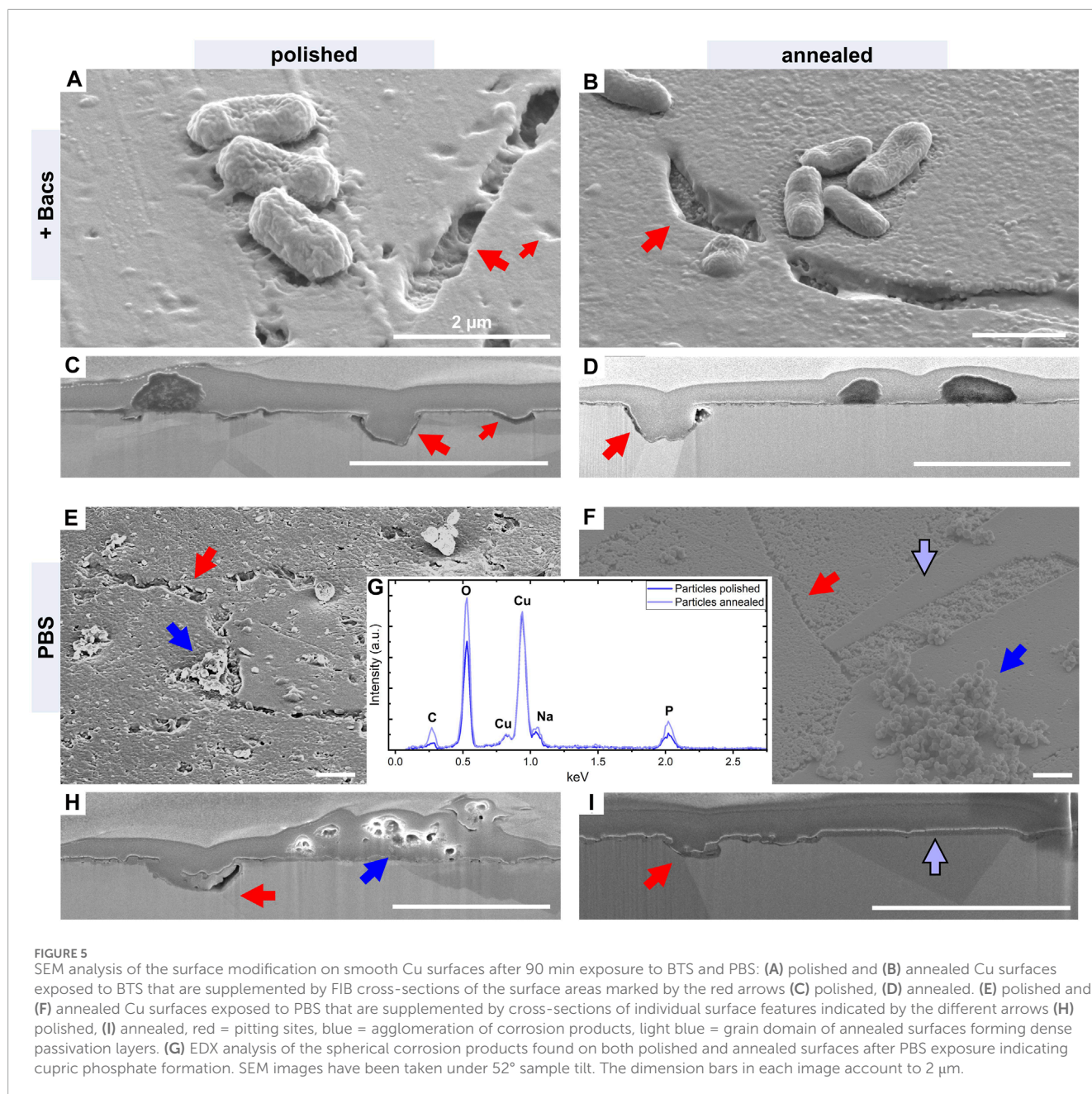
values measured for the initial surface properties, rather than to quantitative Cu ion release, apart from the LS-HT outlier. In fact, hydrophobic wetting properties have previously been shown to have a considerable impact on the antibacterial properties of USP-DLIP surfaces (Müller et al., 2021).

3.3 Characterization of corrosion induced surface modification

Surface modification has been investigated via SEM/FIB after 90 min of exposure to assess the differences in corrosive interaction under exposure to either BTS or pure PBS between the individual surface types related to the variation of Cu ion release. Within the FIB cross-sections, separation between the contrast of bulk Cu and the $\text{Au}_{80}\text{Pd}_{20}$ layer allows to determine the localized thickness of oxidic passivation layers, while surface deterioration by corrosion is parallelly related to the underlying microstructure.

Corrosive surface modification of the reference surfaces has been investigated prior to the USP-DLIP surfaces to gain a basic understanding of the corrosion mechanisms occurring in relation to the differences in the Cu microstructure. Surface deterioration on polished reference surfaces exposed to BTS includes the formation of elongated pits along surface scratches and grain boundaries, as well as smaller localized pits that are randomly distributed on the surface (big/small red arrow in Figures 5A, C). FIB cross-sectioning reveals a thin and unevenly distributed passivation layer, which is locally interrupted at dominant corrosion sites. Localized pitting appears to be linked to individual units of rearranged crystal orientation within the superficial deformation layer of the as-polished reference surfaces. Annealed reference surfaces exhibit similar elongated corrosion pits, but an absence of randomly localized pitting. Here, corrosive interaction appears to focus on grain boundaries eventually including an intragranular attack of single grains (red arrow in Figures 5B, D). The passivation layer formed on annealed reference surfaces is slightly thicker with a higher homogeneity compared to the polished references, but similarly impaired at pitting corrosion sites.

Corrosion under PBS exposure without bacterial involvement follows similar damaging mechanisms of scratch related and randomized pitting in case of polished reference surfaces, while grain boundaries are attacked on both surface types (red arrows in Figures 5E, F, H, I). In both cases, the oxidic passivation layer is thicker, but not homogeneously distributed. Protrusions of the passivation layer are located within single grain domains and especially on localized corrosion sites like grain boundaries. A homogeneous oxide film can solely be determined for single grain domains on annealed surfaces, where a pronounced intragranular pitting can be determined on neighboring grains, as visible in Figures 5F, I (well passivated grain domain is marked by light blue arrows). On both surfaces, clusters of spherical particles can be detected, which do not appear in similarly high concentration during BTS exposure. EDX analysis reveals increased contents of both oxygen and phosphorus (displayed in Figure 5G) indicating the formation of cupric phosphate ($\text{Cu}_3(\text{PO}_4)_2$) on Cu surfaces due to the combined availability of dissolved oxygen, chloride and phosphate-ions under PBS exposure in ambient conditions, according to literature (He et al., 2015).



The grain specific corrosion behavior observed on annealed surfaces indicates the formation of galvanic microcells with anodic and cathodic grain domains. This mechanism can be driven by orientation related differences in corrosion resistance or preferential epitaxial oxide growth as well as a combination of both (Lapeire et al., 2013; Luo et al., 2019a). In case of annealed Cu surfaces under PBS exposure, 100 oriented grain domains have been observed to majorly act as cathodic sites, by which neighboring grains undergo corrosive erosion where 111 oriented grains were observed to exhibit the most pronounced degradation (Lapeire et al., 2013). The deformed superficial microstructure state of polished samples impairs the formation of such clearly defined heterogeneous conditions, by which corrosion is rather focusing localized weak spots of high defect energy (Nikfahm et al.,

2013; Miyamoto, 2016). Similar observations have previously been made on ground and electro-polished Cu surfaces, where the surface deformation state of the former increased localized pitting corrosion, while grain orientation specific corrosion could be observed on the latter surface type (Luo et al., 2019a). Under exposure to BTS, microcell formation on the Cu surfaces appears to be modified by the presence of bacteria, where no grain specific passivation behavior can be observed on the annealed surfaces, while the overall passivation layer exhibits lower thickness for both surface types. Former studies have shown that the re-accumulation of dissolved Cu ions within protective oxide layers on smooth Cu surfaces is largely suppressed by bacterial Cu scavenging (Luo et al., 2019b). Thus, higher Cu release values measured alongside BTS exposure can directly be related to both, a sustained high corrosive

activity by prevention of surface passivation and parallelly increased Cu levels bound within bacterial cells, which are withdrawn by pipetting. The increased formation of cupric phosphate clusters in pure PBS furthermore indicates an excess availability of free Cu ions in vicinity to the substrate surface in the absence of bacteria.

The passivation layer formed on USP-DLIP samples under BTS exposure exhibit low thicknesses akin to the reference samples indicating similar impairment of surface passivation in the presence of bacteria. In contrast, surface deterioration is less obvious on USP-DLIP surfaces, where superficial pitting corrosion can only be observed on LS and HT-LS sample types under BTS exposure. Here, pitting corrosion sites are located within both the topographic peaks as well as the valley regions mostly related to grain boundaries or complete corrosive removal of superficial grain domains. The comparison between Figures 6A, C reveals that pitting sites in valley regions tend to be covered by a superficial passivation layer, while peak related pitting might also be detectable without cross-sectioning mostly due to their exposed location (corrosion sites are indicated by red arrows, the white arrows mark the position of the cross-section taken). Small amounts of spherical Cu phosphate particles can be observed on USP-DLIP surfaces as well with a predominant relation to bacterial remnants (see blue arrows in Figures 6A, C).

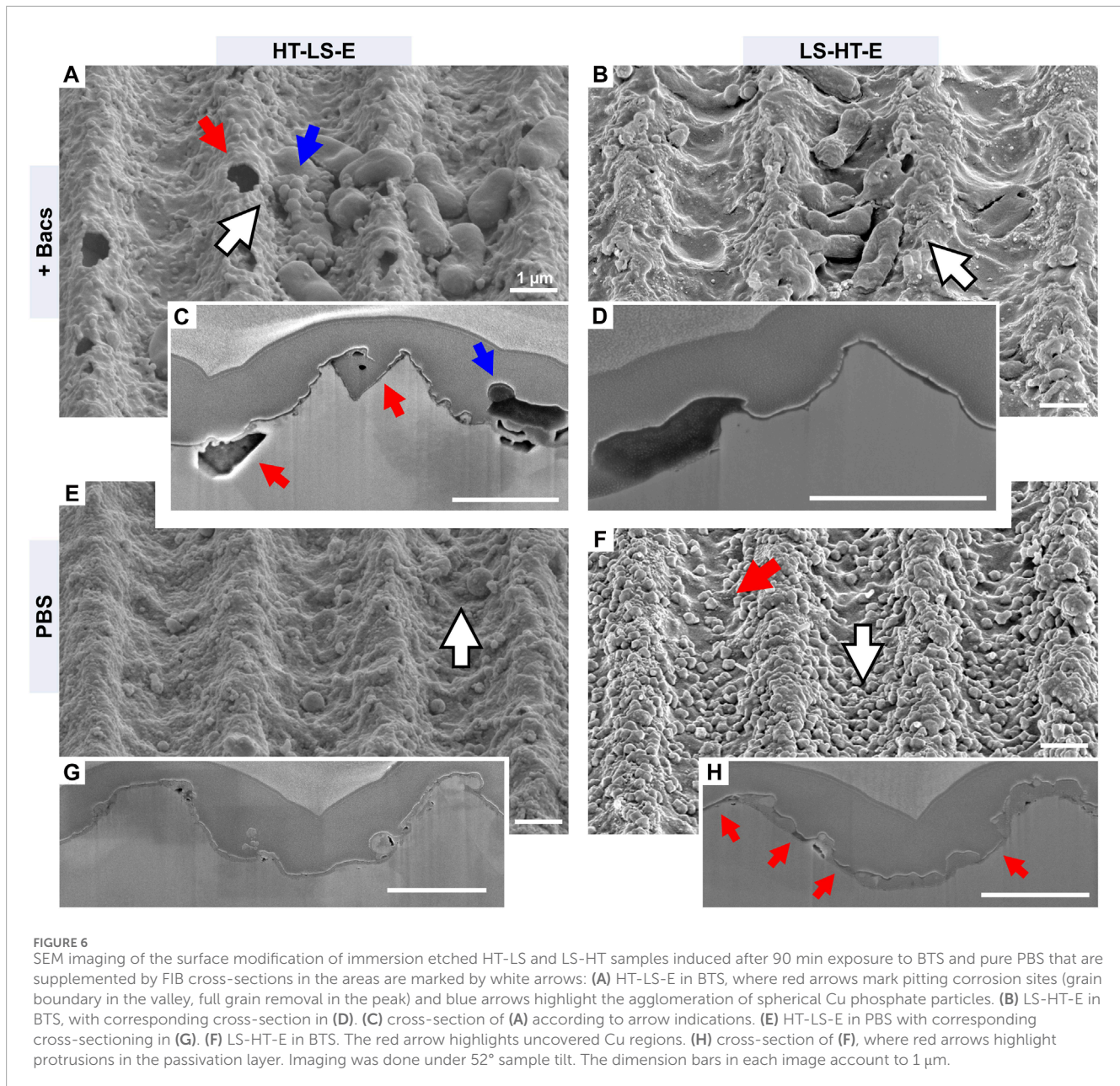
The impact of bacterial presence on surface passivation is further emphasized by comparison to surface modification on corresponding samples exposed to pure PBS, displayed in Figures 6E–H. Both LS and HT-LS samples form a dense passivation layer, which is homogeneously covering the surface. Pitting corrosion sites cannot be determined in SEM analyzation but are revealed by FIB cross-sectioning (an example is provided in Figure 7E). In contrast, surface passivation appears to be heterogeneously distributed on LS-HT surfaces. Here, surface oxide agglomerates appear in separated rather spherical particles that tend to connect by growth instead of a homogeneous layer. The localized accumulations of surface oxide exhibit an increased thickness in comparison to PBS-related passivation layers formed on LS and HT-LS surfaces. Higher quantitative accumulation is observed on peaks compared to valley regions, where yet non-passivated areas of the Cu surface remain uncovered between the agglomerated oxide clusters (red arrows in Figures 6F, H).

An extended comparison between surface passivation under BTS and PBS exposure as well as the initial surface state of the different sample types was conducted by means of FIB cross-section analysis. Representative outtakes of the USP-DLIP related data used in this investigation are illustrated in Figure 7 and summarized in Figure 8A. Aside of both the as-processed LS and HT-LS surfaces, initial oxide thickness of the different surface types ranges below 10 nm with slightly higher values on the USP-DLIP samples. Thickness of the oxide layers on these surfaces further increases alongside BTS and PBS exposure with a clear dominance in PBS due to an unimpaired surface passivation, which is especially striking for the LS-HT samples. These surfaces exhibit the largest gap between BTS and PBS related oxide thicknesses. The high values and standard deviation under PBS exposure are directly linked to the heterogeneous passivation layer formed. The deviating distribution of surface oxide indicates cathodic and anodic surface sites that potentially form galvanic microcells, where resulting impairment of surface passivation can be estimated to account for the continuously

high Cu ion release rate measured via ICP-QQQ. Full passivation might be finally attained on a later point after further oxide growth but is not reached within the experimental time frame applied here. The formation of oxide clusters is majorly suppressed in the presence of bacteria.

In case of PBS exposure, the passivation layer of HT-LS samples is similar to the reference surfaces. The oxide thickness of LS samples tend to range higher but in similar scale to single cathodic grain domains of annealed reference surfaces. Here, the reduced Cu ion release measured on USP-DLIP surfaces indicates higher surface passivation in comparison to the corresponding Cu emission of the reference samples, although the measured oxide thickness accounts to similar values after 90 min of PBS exposure. In parallel, a deviating passivation behavior is observed on as-processed LS and HT-LS surfaces between BTS and PBS exposure. The high initial values measured for these samples are related to the localized surface extension of the flake-like surface oxide accumulated during laser processing (compare Figures 7A, B, M, N). Destabilization of these oxide agglomerations might be assumed to occur during annealing and under BTS exposure, where both as-processed LS and HT-LS surfaces exhibit a decline in oxide layer thickness, while remnants of this oxide structures could not be observed in SEM-analysis after each treatment (see Figures 7A–D, M–P and as-processed HT-LS in Figures 7Y, Z). A dissolution of the flake-like surface oxide structures under BTS exposure might be related to the difference in Cu ion release between the as-processed and etched surface types, as well as the high initial Cu release peak after 30 min of exposure on as-processed HT-LS samples. It can be assumed that the rapid removal of these substructures has a parallel effect on functional properties such as surface wettability, which is emphasized by the extended gap between CA of HT-LS surfaces in as-processed and immersion etched surface state. The resulting accelerated surface wetting appears to account for the absence of a CFU reduction lag on as-processed HT-LS samples within the first 30 min of exposure. In the case of PBS exposure, a strong increase of oxide thickness especially on the peak regions indicates an opposing role in surface corrosion, where the flake-like oxide structures appear to act as nuclei for epitaxial oxide growth, in turn.

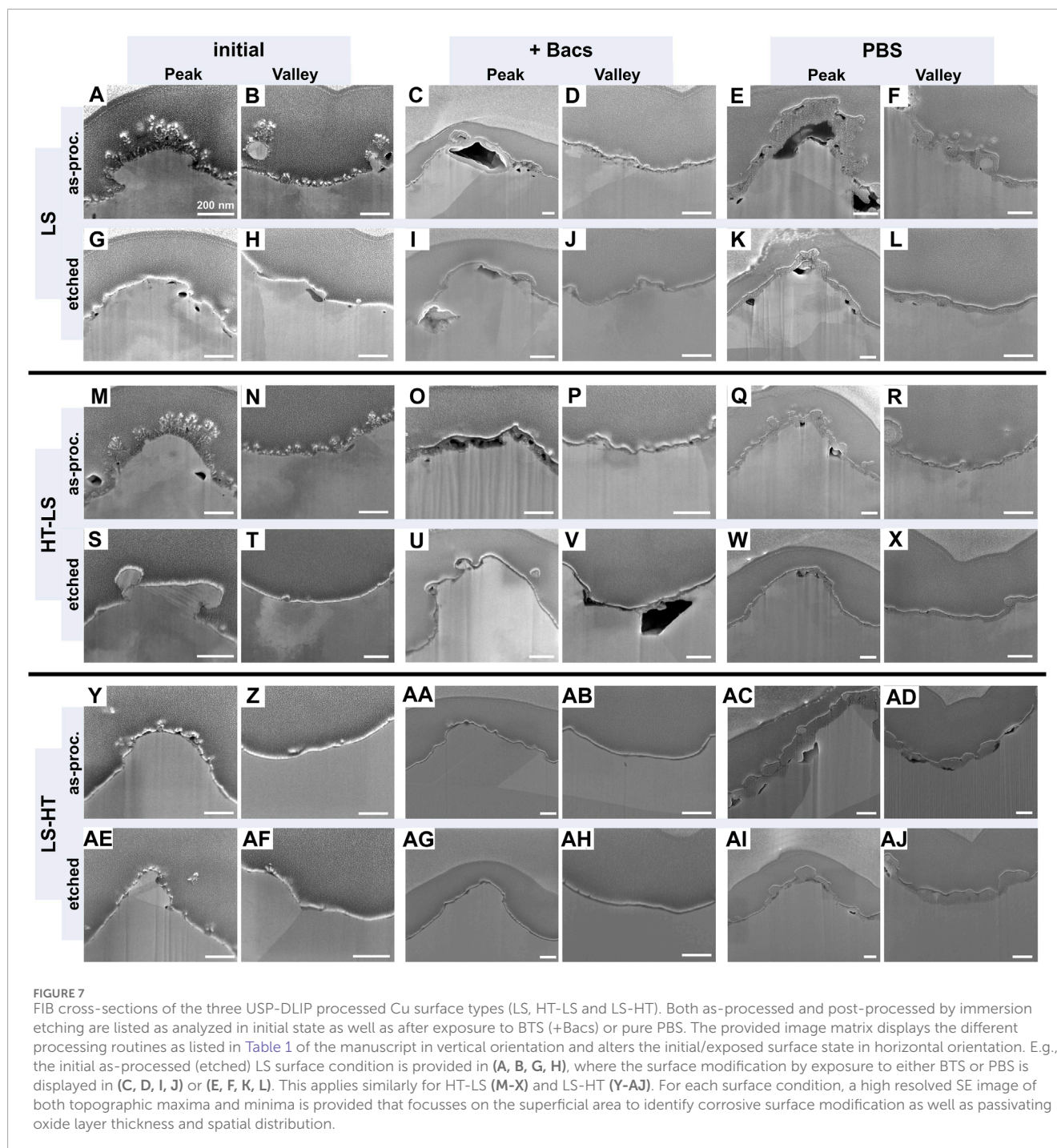
Complementary observations are made via GI-XRD regarding the development of Cu oxide thickness represented by comparison of the Cu_2O 111 peaks as displayed in Figures 8B–D. Cu_2O has been determined as the stabilizing oxide phase predominantly involved in surface passivation of Cu substrates exposed to saline solutions (Luo et al., 2019a), whereas CuO plays a minor role within the interface between Cu_2O and moist/aqueous environments (Platzman et al., 2008). Corresponding to the results of FIB cross-section analysis, the integral intensity of Cu_2O 111 peaks on the USP-DLIP surfaces increases alongside surface exposure to both BTS and PBS, which furthermore indicates a certain amount of oxide formation in the presence of bacteria, as well. This indication of minor surface passivation can be linked to the slight decline in Cu ion release rate after 30 min of exposure, especially on both LS and HT-LS samples. Between these two surface types, oxide thickness continuously ranges higher on LS samples which is accompanied by a slightly higher Cu ion release rate under BTS exposure and quicker passivation in pure PBS. Quantitative oxide formation on LS-HT appears to level in similar magnitude compared to both LS and HT-LS surfaces in spatial distribution. The



high oxide cluster thickness and uncovered surface compartments tend to level out in an overall oxide growth rate closely related to as-processed HT-LS samples.

The observed deviations in surface passivation between the different surface types seem to correspond to the process-induced surface deformation states. Surface deformation by USP-DLIP processing can be linked to rapid and stable surface passivation under PBS exposure as well as reduced Cu release rates per surface area in the presence of bacteria. Previous deformation from polishing additionally appears to impact surface passivation considering the slight difference in oxide thicknesses between LS and HT-LS surfaces after 90 min of PBS exposure. The reference as well as the annealed LS-HT surfaces exhibit lower superficial deformations states, whereas higher Cu release rates under pure PBS exposure indicate a reduced passivation

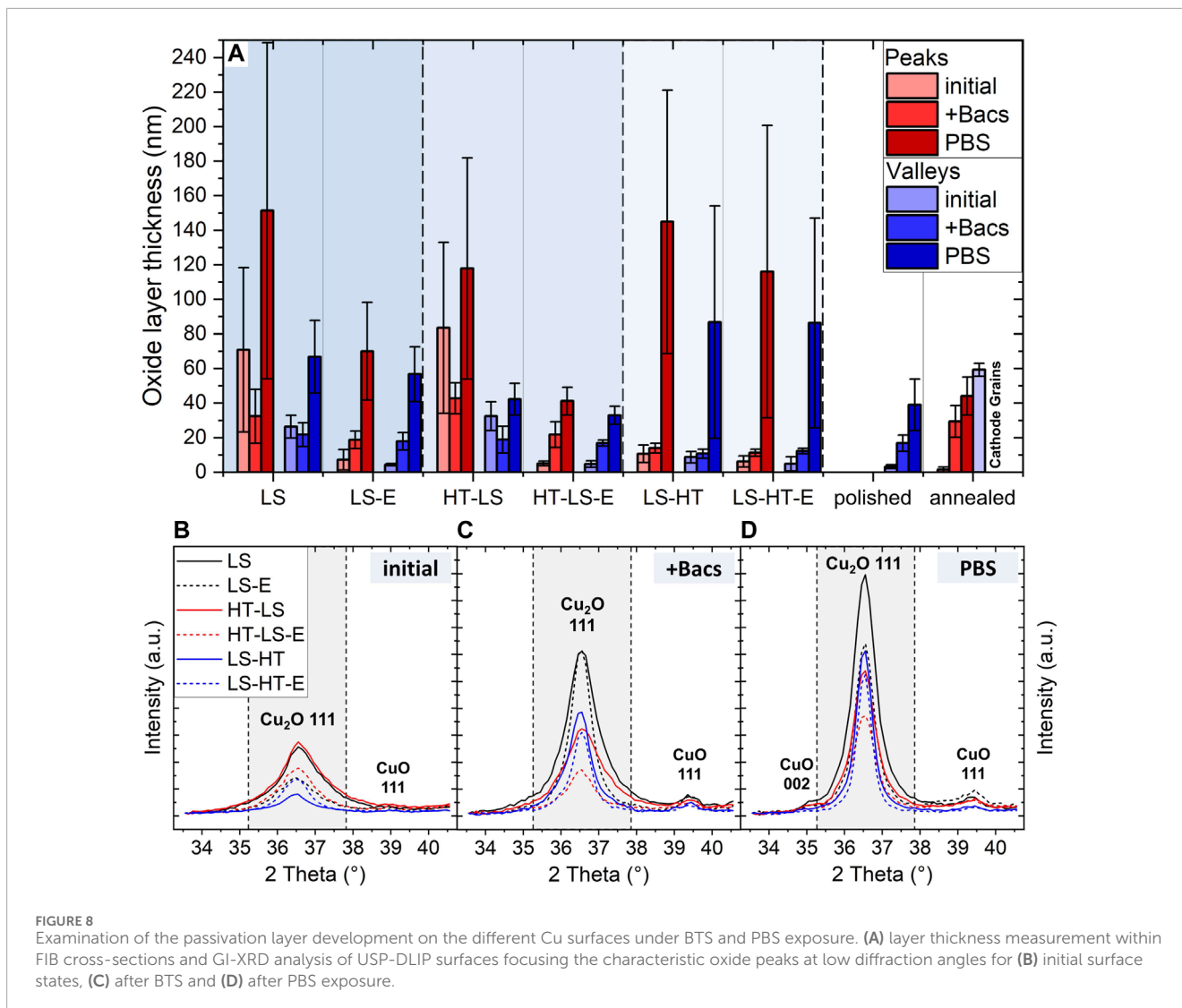
capability in comparison to both LS and HT-LS surfaces. This differentiation in corrosion behavior is counterintuitive according to Ralston's rule, since surface defects including grain boundaries and dislocations are points of attack for Cl^- driven pitting corrosion in saline solutions and should increase the corrosion rate with higher densities (Vinogradov et al., 1999; Miyamoto, 2016; Luo et al., 2019a). However, an alteration of passivation behavior in saline environment was previously described at a certain state of crystallographic deformation that inhibits a clear differentiation between neighboring cathodic and anodic surface sites alongside microcell formation (Miyamoto et al., 2008; Miyamoto, 2016). Corrosion behavior of the Cu surfaces was observed to switch from grain boundary focused and intergranular pitting to uniform surface corrosion, after sufficiently high substrate deformation that results in enhanced surface passivation (Nikfahm et al., 2013). This



is most likely linked to a higher mobility of Cu ions within the dense dislocation network in vicinity to the surface that enables a homogeneous surface passivation, where the lack of breaches prevent further corrosive attack (Miyamoto et al., 2008; Zhao et al., 2014). In Zhang et al. (2014) a comparably high deformation state was reached by high-current electron beam irradiation. The parallelly increased corrosion resistance was linked to the formation of supersaturated dislocation networks alongside short-termed surface melting and crater formation similar to the processing characteristics of USP-DLIP on Cu (Müller et al., 2023). The role

of processed induced surface defects is especially emphasized by comparing corrosion on LS and HT-LS sample types to LS-HT samples, sharing similar topographies but deviating superficial deformation states.

A differentiation between Cu surface types undergoing homogeneous or microcell corrosion is similarly visible when comparing the GI-XRD spectra in Figure 9 before and after exposure to both BTS and PBS. Here, peaks related to the Cu 200, 220 and 311 orientations get weakened for both LS-HT and the annealed reference samples, while a minor decline of Cu 220 can also be



observed for the polished reference. The deviations between initial and as-exposed XRD-spectra indicates a shift in the texture of the near-surface microstructure by corrosive erosion of anodic grain domains. This reduction is most expressed in BTS exposure, where impaired passivation induces a higher corrosive rate, but can also be observed in PBS exposure for LS-HT and annealed surfaces. The Cu 220 signal undergoes the most pronounced decline during exposure, which might be linked to its relation to the Cu 111 surface oriented microstructure compartments exhibiting the highest erosion within microcell corrosion between neighboring grain domains (Lapeire et al., 2013). Aside from HT-LS-E that also shows a mild change of the GI-XRD spectrum under BTS exposure, LS and HT-LS surfaces do not exhibit deviants of superficial crystallography after BTS and PBS exposure, which indicates a corrosion mechanism that is rather indifferent of grain orientation.

Independent of the deformation state of the substrate surface, the line-like surface topography generated via USP-DLIP processing appears to impact localized surface passivation, since oxide thickness is found to be constantly higher on peak compared to valley regions. This might be influenced by topographic effects with different possible underlying mechanisms: On the one hand,

valley regions tend to be shadowed in case of galvanically induced material flows. On the other hand, the higher surface/volume ratio in the peak regions rather exposes grain subdivisions and might influence the local electric fields leading to topographically induced microcell formation. Grains located within the pattern peaks additionally exhibit an enlarged and convex shaped surface leading to an exposure of differing crystallographic orientations of the same grain to corrosive attack. This might drive the increase of pitting corrosion in the peak regions on LS and HT-LS samples partly inducing topographic erosion in case of BTS exposure, while unimpaired passivation leads to thicker passivation layers.

4 Conclusion

The influence of microstructure modification on the antimicrobial properties of Cu surfaces has been investigated by means of a dissemination of the different surface deformation sources throughout sample preparation including topographical patterning via USP-DLIP.

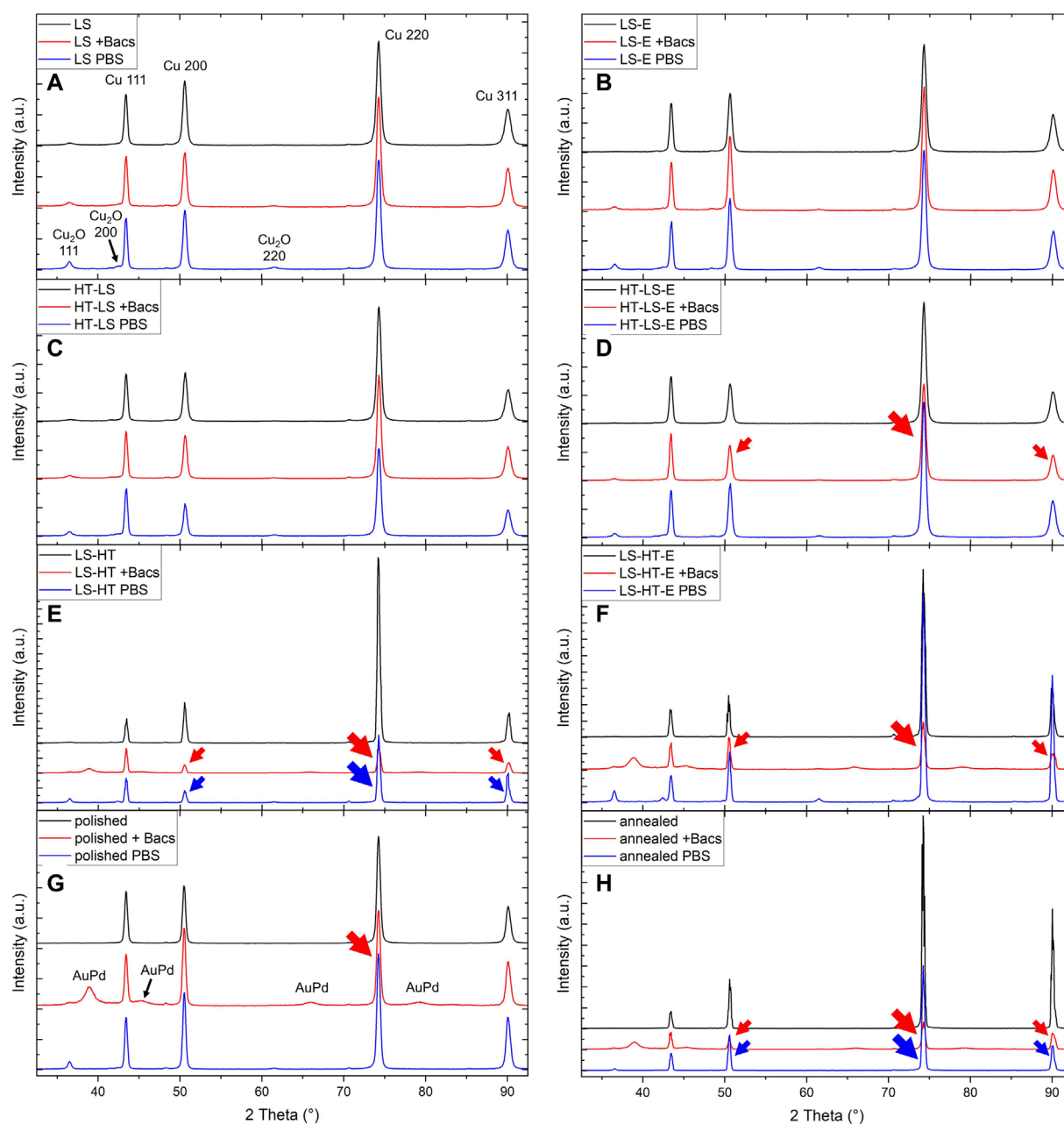


FIGURE 9

Comparison of the GI-XRD spectra between the initial and the BTS/PBS exposed Cu surface types for (A) LS, (B) LS-E, (C) HT-LS, (D) HT-LS-E, (E) LS-HT, (F) LS-HT-E, (G) polished and (H) annealed surfaces. Red and blue arrows mark a reduction of peak intensities for either BTS or PBS exposed samples. In case of (E-H) the BTS samples additionally exhibit side peaks from the 10 nm Au80Pd20 coating.

- **Initial state of the superficial microstructure:** The initial microstructure of the Cu substrate exhibits a characteristic cold-rolled texture with a dominance of grain domains in 100 orientation parallel to the surface. Annealing induces a mild increase of 111 domains. USP-DLIP processing does not affect the texture of bulk or superficial microstructure in case of LS and LS-HT, whereas the superficial texture of previously annealed Cu surfaces gets modified in the case of HT-LS samples. Regarding overall deformation state, the surface types can be subdivided in LS > HT-LS >> polished >> LS-HT >

annealed. Different impacts of the microstructure deformation state on functional surface properties are observed:

- **Surface wettability corresponding to topography and microstructure state:** The wetting behavior of the different Cu surface types appears to be highly impacted by surface topography befitting to the Wenzel law (Wenzel, 1949). The near-surface microstructure modification by USP-DLIP processing appears to additionally impact the level of the developed hydrophobicity. This is especially emphasized comparing the CA of the different immersion etched USP-DLIP

surface types that exhibit identical surface topography. Near-surface defect density furthermore seems to influence surface passivation, which might similarly include quantitative carbon-group absorption, according to recent findings (Löflein et al., 2023). A higher hydrophobicity can consistently be observed on as-processed surface states, which is related to process-induced oxidic sub-structures in the case of LS and HT-LS surfaces. A dissolution of the delicate oxide structures in BTS solution might lead to a rapid increase in surface wettability, in turn, that appears to facilitate early state bacteria/surface contact on HT-LS samples.

- **Impact on corrosive interaction:** Exposure to PBS solution with and without bacteria induces surface corrosion that alters between the different surface types directly dependent on superficial microstructure deformation. Corrosive interaction in pure PBS is subdivided into homogeneous oxide growth leading to stabilizing passivation for LS and HT-LS samples and heterogeneous surface degradation alongside minor surface passivation in the case of the reference and LS-HT surfaces. The driving mechanism behind heterogeneous surface corrosion is galvanic microcell formation between cathodic low energetic and anodic high energetic surface sites, linked to surface defects like scratches as well as grain boundaries and neighboring grain orientations. A sacrificial erosion of certain grain orientation is further suggested by a deviation in GI-XRD signal distribution after both BTS and PBS exposure. On LS and HT-LS samples, a clear spatial separation between cathodic and anodic surface sites appears to be impeded due to the high superficial defect densities, which leads to homogeneous corrosion and oxide growth that enables stabilizing passivation. Surface passivation is inhibited in the presence of bacteria, whereby the acting corrosion mechanisms might slightly deviate from pure PBS, also enabling localized pitting. Quantitative Cu ion release is found to be directly linked to the passivation capabilities of the different surface types in either BTS or PBS environment. Cu emission of LS and HT-LS samples solely surpasses the reference surfaces because of their higher surface/area ratio. Aside from the mentioned indications of microcell formation, an additional impact of surface topography on localized oxide agglomeration is apparent independent on the superficial microstructure.
- **Antimicrobial efficiency:** Bacterial viability on the different Cu surfaces is found to be indirectly influenced by the process-induced deformation state of the superficial microstructure due to its impact on functional surface properties like surface wettability and corrosive interaction. Overall bacterial deactivation assessed after 90 min of exposure exhibits an enhanced reduction of viable bacteria on all tested USP-DLIP surfaces than ranges between 4 and >12 times below CFU-values of the smooth references. A consistently high killing efficiency is achieved on LS surface types independent of their post-processing state, whereas HT-LS levels above LS-HT both in the as-processed and immersion etched state. Probably due to increased Cu ion release by dissolution of the flake-like surface agglomerations, as-processed samples exhibit higher bacterial killing than their immersion etched counter parts. Nevertheless, the bactericidal efficiency against *E. coli* appears to correlate more with surface wettability than quantitative

Cu release, since CFU-decrease on the individual Cu surfaces scales inversely with their respective initial state CA-values, aside of the LS-HT outlier. Here, surface hydrophobicity and antimicrobial efficiency is supported by USP-DLIP induced defect implantation in contrast to the parallelly increased surface passivation capabilities that reduce the quantitative Cu emission. In accordance with previous findings (Müller et al., 2021), this indicates that physio-chemical surface properties and their influence on bacterial surface interaction play a similarly important role in the antimicrobial efficiency of Cu surface as the actual quantity of Cu ion release.

The presented results illustrate how integrated Cu surface properties are influenced by USP-DLIP processing, achieving complementing functional features that benefit the application scope. In the case of antimicrobial Cu surfaces, the USP-DLIP induced modification of both superficial chemistry and microstructure alongside surface topography were found to improve bactericidal efficiency in mutual interaction, whereby neutralization of one or two of these impacts decreases bactericidal efficiency against *E. coli*. This is a good example of how targeted surface optimization involving multi-level substrate modification can be tailored to provide the greatest benefit for a specific application.

Data availability statement

The raw data supporting the conclusions of this article will be made available by the authors, without undue reservation.

Author contributions

DM: Conceptualization, Data curation, Formal Analysis, Funding acquisition, Investigation, Methodology, Project administration, Software, Validation, Visualization, Writing—original draft, Writing—review and editing. BJ: Investigation, Writing—review and editing. SW: Investigation, Writing—review and editing. CP: Data curation, Formal Analysis, Investigation, Methodology, Software, Writing—review and editing. SS: Data curation, Formal Analysis, Investigation, Methodology, Software, Writing—review and editing. KB: Data curation, Formal Analysis, Investigation, Methodology, Software, Writing—review and editing. RK: Funding acquisition, Resources, Supervision, Writing—review and editing. FM: Funding acquisition, Resources, Supervision, Writing—review and editing.

Funding

The author(s) declare that financial support was received for the research, authorship, and/or publication of this article. This work has been funded by the German Research Foundation (DFG) within the project “Controlled bacterial interaction to increase the antimicrobial efficiency of copper surfaces” (project number 415956642) as well as the German Aerospace Center—Space Administration (DLR) within the project “Investigation of antimicrobial metal surfaces under space conditions—An effective

strategy to prevent microbial biofilm formation” (project number 50WB1930). The authors acknowledge financial support in the project “MatInnovat” supported by the Saarland State Ministry of Economics with resources from the European Fund for Regional Development (EFRE) and funding by the German Research Foundation for the PFIB/SEM instrument used for the EBSD measurements (DFG, INST 256/510-1 FUGG) and for the ICP-QQQ instrument used for elemental quantification (DFG, INST 256/553-1 FUGG).

Acknowledgments

We would like to acknowledge the support of Prof. Rolf Müller and his group from the Helmholtz Institute for Pharmaceutical Research Saarland (HIPS) by providing the *E.coli* K12 strain, which was used to assess the antimicrobial properties of the differently treated Cu surfaces via wet plating.

References

- Ahmed, A. S., Müller, D. W., Bruyere, S., Holtsch, A., Müller, F., Barrirero, J., et al. (2023). Surface modification of brass via ultrashort pulsed direct laser interference patterning and its effect on bacteria-substrate interaction. *ACS Appl. Mat. Interfaces* 15, 36908–36921. doi:10.1021/acsami.3c04801
- Boinovich, L. B., Kaminsky, V. V., Domantovsky, A. G., Emelyanenko, K. A., Aleshkin, A. V., Zulkarneev, E. R., et al. (2019). Bactericidal activity of superhydrophobic and superhydrophilic copper in bacterial dispersions. *Langmuir* 35, 2832–2841. doi:10.1021/acs.langmuir.8b03817
- Boinovich, L. B., Modin, E. B., Aleshkin, A. V., Emelyanenko, K. A., Zulkarneev, E. R., Kiseleva, I. A., et al. (2018). Effective antibacterial nanotextured surfaces based on extreme wettability and bacteriophage seeding. *ACS Appl. Nano Mat.* 1, 1348–1359. doi:10.1021/acsanm.8b00090
- Cámara, M., Green, W., MacPhee, C. E., Rakowska, P. D., Raval, R., Richardson, M. C., et al. (2022). Economic significance of biofilms: a multidisciplinary and cross-sectoral challenge. *Npj Biofilms Microbiomes* 8, 42–48. doi:10.1038/s41522-022-00306-y
- Cullity, B. D., and Stock, S. R. (2001). *Elements of X-ray diffraction*.
- Emelyanenko, A. M., Pytskii, I. S., Kaminsky, V. V., Chulkova, E. V., Domantovsky, A. G., Emelyanenko, K. A., et al. (2020). Superhydrophobic copper in biological liquids: antibacterial activity and microbiologically induced or inhibited corrosion. *Colloids Surfaces B Biointerfaces* 185, 110622. doi:10.1016/j.colsurfb.2019.110622
- Epperlein, N., Menzel, F., Schwibbert, K., Koter, R., Bonse, J., Sameith, J., et al. (2017). Influence of femtosecond laser produced nanostructures on biofilm growth on steel. *Appl. Surf. Sci.* 418, 420–424. doi:10.1016/j.apsusc.2017.02.174
- Fadeeva, E., Truong, V. K., Stiesch, M., Chichkov, B. N., Crawford, R. J., Wang, J., et al. (2011). Bacterial retention on superhydrophobic titanium surfaces fabricated by femtosecond laser ablation. *Langmuir* 27, 3012–3019. doi:10.1021/la104607g
- Hans, M., Erbe, A., Mathews, S., Chen, Y., Solioz, M., and Mücklich, F. (2013). Role of copper oxides in contact killing of bacteria. *Langmuir* 29, 16160–16166. doi:10.1021/la404091z
- Hans, M., Támara, J. C., Mathews, S., Bax, B., Hegetschweiler, A., Kautenburger, R., et al. (2014). Laser cladding of stainless steel with a copper-silver alloy to generate surfaces of high antimicrobial activity. *Appl. Surf. Sci.* 320, 195–199. doi:10.1016/j.apsusc.2014.09.069
- He, G., Hu, W., and Li, C. M. (2015). Spontaneous interfacial reaction between metallic copper and PBS to form cupric phosphate nanoflower and its enzyme hybrid with enhanced activity. *Colloids Surfaces B Biointerfaces* 135, 613–618. doi:10.1016/j.colsurfb.2015.08.030
- Kimkes, T., and Heinemann, M. (2020). How bacteria recognise and respond to surface contact. *FEMS Microbiol. Rev.* 44, 106–122. doi:10.1093/femsre/fuz029
- Lapeire, L., Martinez Lombardia, E., Verbeken, K., De Graeve, I., Kestens, L. A. I., and Terry, H. (2013). Effect of neighboring grains on the microscopic corrosion behavior of a grain in polycrystalline copper. *Corros. Sci.* 67, 179–183. doi:10.1016/j.corsci.2012.10.017
- Löflein, S. M., Kasper, M., Merz, R., Pauly, C., Müller, D. W., Kopnarski, M., et al. (2021). Patience Alone is not Enough - A Guide for the Preparation of Low-Defect Sections from Pure Copper Geduld allein reicht nicht! - Ein Leitfaden

Conflict of interest

Authors DM and SW were employed by SurFunction GmbH. The remaining authors declare that the research was conducted in the absence of any commercial or financial relationships that could be construed as a potential conflict of interest.

Publisher's note

All claims expressed in this article are solely those of the authors and do not necessarily represent those of their affiliated organizations, or those of the publisher, the editors and the reviewers. Any product that may be evaluated in this article, or claim that may be made by its manufacturer, is not guaranteed or endorsed by the publisher.

zur Herstellung defektarmer Schlitze von Reinkupfer. *Prakt. Metallogr. Metallogr.* 58, 388–407. doi:10.1515/pm-2021-0031

Löflein, S. M., Merz, R., Müller, D. W., Kopnarski, M., and Mücklich, F. (2022). An in-depth evaluation of sample and measurement induced influences on static contact angle measurements. *Sci. Rep.* 12, 19389–19416. doi:10.1038/s41598-022-23341-3

Löflein, S. M., Merz, R., Müller, D. W., Kopnarski, M., and Mücklich, F. (2023). The influence of adventitious carbon groups on the wetting of copper: a study on the effect of microstructure on the static contact angle. *Langmuir* 39, 12020–12031. doi:10.1021/acs.langmuir.3c01060

Luo, J., Hein, C., Ghanbaja, J., Pierson, J., and Mücklich, F. (2019b). Bacteria accumulate copper ions and inhibit oxide formation on copper surface during antibacterial efficiency test. *Micron* 127, 102759. doi:10.1016/j.micron.2019.102759

Luo, J., Hein, C., Pierson, J., and Mücklich, F. (2019a). Localised corrosion attacks and oxide growth on copper in phosphate-buffered saline. *Mat. Charact.* 158, 109985. doi:10.1016/j.matchar.2019.109985

Maikranz, E., Spengler, C., Thewes, N., Thewes, A., Nolle, F., Jung, P., et al. (2020). Different binding mechanisms of *Staphylococcus aureus* to hydrophobic and hydrophilic surfaces. *Nanoscale* 12, 19267–19275. doi:10.1039/d0nr03134h

Meister, T. L., Fortmann, J., Breisch, M., Sengstock, C., Steinmann, E., Köller, M., et al. (2022). Nanoscale copper and silver thin film systems display differences in antiviral and antibacterial properties. *Sci. Rep.* 12, 7193–7210. doi:10.1038/s41598-022-11212-w

Mikolay, A., Huggett, S., Tikana, L., Grass, G., Braun, J., and Nies, D. H. (2010). Survival of bacteria on metallic copper surfaces in a hospital trial. *Appl. Microbiol. Biotechnol.* 87, 1875–1879. doi:10.1007/s00253-010-2640-1

Miyamoto, H. (2016). Corrosion of ultrafine grained materials by severe plastic deformation, an overview. *Mat. Trans.* 57, 559–572. doi:10.2320/matertrans.M2015452

Miyamoto, H., Harada, K., Mimaki, T., Vinogradov, A., and Hashimoto, S. (2008). Corrosion of ultra-fine grained copper fabricated by equal-channel angular pressing. *Corros. Sci.* 50, 1215–1220. doi:10.1016/j.corsci.2008.01.024

Molteni, C., Abicht, H. K., and Solioz, M. (2010). Killing of bacteria by copper surfaces involves dissolved copper. *Appl. Environ. Microbiol.* 76, 4099–4101. doi:10.1128/AEM.00424-10

Müller, D. W., Fox, T., Grützmacher, P. G., Suarez, S., and Mücklich, F. (2020a). Applying ultrashort pulsed direct laser interference patterning for functional surfaces. *Sci. Rep.* 10, 3647. doi:10.1038/s41598-020-60592-4

Müller, D. W., Holtsch, A., Löflein, S., Pauly, C., Spengler, C., Grandthyll, S., et al. (2020b). In-depth investigation of copper surface chemistry modification by ultrashort pulsed direct laser interference patterning. *Langmuir* 36, 13415–13425. doi:10.1021/acs.langmuir.0c01625

Müller, D. W., Löflein, S., Pauly, C., Briesenick, M., Kickelbick, G., and Mücklich, F. (2023). Multi-pulse agglomeration effects on ultrashort pulsed direct laser interference patterning of Cu. *Appl. Surf. Sci.* 611, 155538. doi:10.1016/j.apsusc.2022.155538

Müller, D. W., Löflein, S., Terriac, E., Brix, K., Kautenburger, R., Siems, K., et al. (2021). Increasing antibacterial efficiency of Cu surfaces by targeted surface functionalization via ultrashort pulsed direct laser interference patterning. *Adv. Mat. Interfaces.* 8, 2001656. doi:10.1002/admi.202001656

- Nikfahm, A., Danaee, I., Ashrafi, A., and Toroghinejad, M. R. (2013). Effect of grain size changes on corrosion behavior of copper produced by accumulative roll bonding process. *Mat. Res.* 16, 1379–1386. doi:10.1590/S1516-14392013005000135
- Peter, A., Lutey, A. H. A., Faas, S., Romoli, L., Onuseit, V., and Graf, T. (2020). Direct laser interference patterning of stainless steel by ultrashort pulses for antibacterial surfaces. *Opt. Laser Technol.* 123, 105954. doi:10.1016/j.optlastec.2019.105954
- Platzman, I., Brener, R., Haick, H., and Tannenbaum, R. (2008). Oxidation of polycrystalline copper thin films at ambient conditions. *J. Phys. Chem. C* 112, 1101–1108. doi:10.1021/jp076981k
- Pratt, L. A., and Kolter, R. (1998). Genetic analysis of *Escherichia coli* biofilm formation: roles of flagella, motility, chemotaxis and type I pili. *Mol. Microbiol.* 30, 285–293. doi:10.1046/j.1365-2958.1998.01061.x
- Razavipour, M., Gonzalez, M., Singh, N., Cimenci, C. E., Chu, N., Alarcon, E. I., et al. (2022). Biofilm inhibition and antiviral response of cold sprayed and shot peened copper surfaces: effect of surface morphology and microstructure. *J. Therm. Spray Technol.* 31, 130–144. doi:10.1007/s11666-021-01315-7
- Schneider, C. A., Rasband, W. S., and Eliceiri, K. W. (2012). NIH Image to ImageJ: 25 years of image analysis. *Nat. Methods.* 9, 671–675. doi:10.1038/nmeth.2089
- Siems, K., Müller, D. W., Maertens, L., Ahmed, A., Van Houdt, R., Mancinelli, R. L., et al. (2022). Testing laser-structured antimicrobial surfaces under space conditions: the design of the ISS experiment BIOFILMS. *Technol.* 2, 1–18. doi:10.3389/frspt.2021.773244
- Smith, J. L., Tran, N., Song, T., Liang, D., and Qian, M. (2022). Robust bulk micro-nano hierarchical copper structures possessing exceptional bactericidal efficacy. *Biomaterials* 280, 121271. doi:10.1016/j.biomaterials.2021.121271
- Sobisch, L.-Y., Rogowski, K. M., Fuchs, J., Schmieder, W., Vaishampayan, A., Oles, P., et al. (2019). Biofilm forming antibiotic resistant gram-positive pathogens isolated from surfaces on the international space station. *Front. Microbiol.* 10, 543–616. doi:10.3389/fmicb.2019.00543
- Tripathy, A., Sen, P., Su, B., and Briscoe, W. H. (2017). Natural and bioinspired nanostructured bactericidal surfaces. *Adv. Colloid Interface Sci.* 248, 85–104. doi:10.1016/j.cis.2017.07.030
- Vincenc Oboña, J., Ocelik, V., Rao, J. C., Skolski, J. Z. P., Römer, G. R. B. E., Huis In 't Veld, A. J., et al. (2014). Modification of Cu surface with picosecond laser pulses. *Appl. Surf. Sci.* 303, 118–124. doi:10.1016/j.apsusc.2014.02.104
- Vinogradov, A., Mimaki, T., Hashimoto, S., and Valiev, R. (1999). On the corrosion behaviour of ultra-fine grain copper. *Scr. Mat.* 41, 319–326. doi:10.1016/S1359-6462(99)00170-0
- Wenzel, R. N. (1949). Surface roughness and contact angle. *J. Phys. Colloid Chem.* 53, 1466–1467. doi:10.1021/j150474a015
- Xiong, Q., Li, Z., and Kitamura, T. (2017). Effect of crystal orientation on femtosecond laser-induced thermomechanical responses and spallation behaviors of copper films. *Sci. Rep.* 7, 9218–9314. doi:10.1038/s41598-017-09559-6
- Yi, G., Riduan, S. N., Armugam, A., Ong, J. T., Hon, P. Y., Abdad, M. Y., et al. (2021). Nanostructured copper surface kills ESKAPE pathogens and viruses in minutes. *ChemMedChem* 16, 3553–3558. doi:10.1002/cmde.202100504
- Zea, L., Mclean, R. J. C., Rook, T. A., Angle, G., Carter, D. L., Delegard, A., et al. (2020). Potential biofilm control strategies for extended space flight missions. *Biofilm* 2, 100026. doi:10.1016/j.biofilm.2020.100026
- Zhang, Z., Yang, S., Lv, P., Li, Y., Wang, X., Hou, X., et al. (2014). The microstructures and corrosion properties of polycrystalline copper induced by high-current pulsed electron beam. *Appl. Surf. Sci.* 294, 9–14. doi:10.1016/j.apsusc.2013.12.178
- Zhao, Y., Cheng, I. C., Kassner, M. E., and Hodge, A. M. (2014). The effect of nanotwins on the corrosion behavior of copper. *Acta Mater.* 67, 181–188. doi:10.1016/j.actamat.2013.12.030